Table 3. For each couple of quantities we list the Spearman's rank correlation coefficient, the corresponding uncertainty, and the number of clusters used to calculate the correlation coefficient.

Parameter	$W_{C\,F275W,\,F336W,\,F438W}$	$\Delta W_{C\,F275W,\,F336W,\,F438W}$	$W^*_{C\,F275W,\,F336W,\,F438W}$	$\Delta W^*_{C\,F275W,\,F336W,\,F438W}$	$W_{F275W,\,F814W}$	$\Delta W_{F275W,\,F814W}$
σ_V	0.30 ± 0.14, 57	0.63 ± 0.08, 57	0.20 ± 0.15, 56	0.54 ± 0.10, 56	0.35 ± 0.14, 57	0.46 ± 0.12, 57
c	0.23 ± 0.14, 57	0.38 ± 0.13, 57	0.18 ± 0.14, 56	0.36 ± 0.13, 56	0.17 ± 0.14, 57	0.31 ± 0.12, 57
μ_V	−0.44 ± 0.12, 57	−0.61 ± 0.09, 57	−0.37 ± 0.12, 56	−0.56 ± 0.11, 56	−0.41 ± 0.13, 57	−0.48 ± 0.10, 57
ϵ	0.08 ± 0.12, 57	−0.02 ± 0.14, 57	−0.07 ± 0.13, 56	−0.04 ± 0.14, 56	0.08 ± 0.14, 57	0.15 ± 0.14, 57
ρ_0	0.44 ± 0.12, 57	0.51 ± 0.12, 57	0.37 ± 0.14, 56	0.45 ± 0.12, 56	0.39 ± 0.13, 57	0.41 ± 0.12, 57
$\log\tau_c$	−0.22 ± 0.15, 57	−0.14 ± 0.15, 57	−0.19 ± 0.14, 56	−0.12 ± 0.15, 56	−0.07 ± 0.15, 57	0.01 ± 0.14, 57
$\log\tau_{hm}$	−0.18 ± 0.15, 57	0.17 ± 0.13, 57	−0.17 ± 0.15, 56	0.19 ± 0.14, 56	−0.01 ± 0.15, 57	0.26 ± 0.13, 57
R_{GC}	−0.38 ± 0.12, 57	0.02 ± 0.13, 57	−0.41 ± 0.12, 56	0.01 ± 0.13, 56	−0.30 ± 0.11, 57	0.01 ± 0.13, 57
age (MF09)	−0.31 ± 0.12, 56	0.07 ± 0.13, 56	−0.26 ± 0.12, 55	0.11 ± 0.13, 55	−0.26 ± 0.12, 56	−0.05 ± 0.14, 56
age (D10)	−0.41 ± 0.11, 56	0.06 ± 0.15, 56	−0.39 ± 0.11, 55	0.11 ± 0.14, 55	−0.29 ± 0.13, 56	0.11 ± 0.15, 56
age (V13)	−0.54 ± 0.09, 51	0.17 ± 0.14, 51	−0.53 ± 0.10, 51	0.18 ± 0.15, 51	−0.51 ± 0.10, 51	0.01 ± 0.15, 51
[Fe/H]	0.79 ± 0.05, 57	−0.07 ± 0.14, 57	0.79 ± 0.05, 56	−0.11 ± 0.14, 56	0.65 ± 0.09, 57	−0.03 ± 0.14, 57
M_V	−0.38 ± 0.12, 57	−0.70 ± 0.07, 57	−0.29 ± 0.14, 56	−0.64 ± 0.09, 56	−0.50 ± 0.12, 57	−0.68 ± 0.08, 57
$\log\mathcal{M}/\mathcal{M}_\odot$	0.60 ± 0.12, 44	0.74 ± 0.08, 44	0.51 ± 0.13, 43	0.68 ± 0.10, 43	0.65 ± 0.12, 44	0.69 ± 0.09, 44
f_{bin}^{C}	0.18 ± 0.17, 34	−0.40 ± 0.15, 34	0.23 ± 0.17, 34	−0.32 ± 0.15, 34	0.12 ± 0.18, 34	−0.36 ± 0.14, 34
f_{bin}^{C-HM}	−0.08 ± 0.15, 46	−0.44 ± 0.12, 46	−0.06 ± 0.15, 46	−0.42 ± 0.13, 46	−0.13 ± 0.16, 46	−0.42 ± 0.11, 46
f_{bin}^{oHM}	−0.29 ± 0.16, 42	−0.51 ± 0.13, 42	−0.22 ± 0.16, 41	−0.44 ± 0.13, 41	−0.26 ± 0.15, 42	−0.37 ± 0.14, 42
$S_{RRLyrae}$	−0.24 ± 0.12, 57	0.02 ± 0.15, 57	−0.26 ± 0.13, 56	−0.01 ± 0.15, 56	−0.23 ± 0.13, 57	−0.14 ± 0.14, 57
$E(B-V)$	0.34 ± 0.12, 57	−0.11 ± 0.14, 57	0.31 ± 0.12, 56	0.06 ± 0.14, 56	0.41 ± 0.12, 57	0.22 ± 0.14, 57
N_1/N_{TOT}	−0.41 ± 0.12, 54	−0.61 ± 0.09, 54	−0.32 ± 0.13, 53	−0.54 ± 0.10, 53	−0.44 ± 0.12, 54	−0.56 ± 0.09, 54

Parameter	$W^*_{F275W,\,F814W}$	$\Delta W^*_{F275W,\,F814W}$	N_1/N_{TOT}	$W^{1G}_{F275W,\,F814W}$	$W^{2G}_{F275W,\,F814W}$
σ_V	0.26 ± 0.14, 56	0.39 ± 0.13, 56	−0.63 ± 0.09, 54	0.12 ± 0.15, 53	0.39 ± 0.13, 53
c	0.17 ± 0.14, 56	0.32 ± 0.12, 56	−0.54 ± 0.11, 54	0.08 ± 0.17, 53	0.18 ± 0.14, 53
μ_V	−0.38 ± 0.13, 56	−0.46 ± 0.11, 56	0.71 ± 0.07, 54	−0.19 ± 0.14, 53	−0.42 ± 0.12, 53
ϵ	0.07 ± 0.13, 56	0.13 ± 0.13, 56	−0.07 ± 0.14, 54	0.15 ± 0.14, 53	0.24 ± 0.13, 53
ρ_0	0.37 ± 0.14, 56	0.39 ± 0.12, 56	−0.63 ± 0.09, 54	0.11 ± 0.15, 53	0.37 ± 0.13, 53
$\log\tau_c$	−0.08 ± 0.15, 56	−0.01 ± 0.14, 56	0.26 ± 0.15, 54	0.04 ± 0.16, 53	0.03 ± 0.15, 53
$\log\tau_{hm}$	−0.03 ± 0.15, 56	0.26 ± 0.13, 56	−0.14 ± 0.15, 54	0.20 ± 0.16, 53	0.17 ± 0.16, 53
R_{GC}	−0.29 ± 0.14, 56	0.02 ± 0.14, 56	−0.05 ± 0.13, 54	0.02 ± 0.16, 53	−0.24 ± 0.13, 55
age (MF09)	−0.25 ± 0.13, 55	−0.01 ± 0.14, 55	0.11 ± 0.15, 53	−0.36 ± 0.11, 52	−0.08 ± 0.12, 52
age (D10)	−0.30 ± 0.12, 55	0.16 ± 0.15, 55	0.08 ± 0.13, 53	−0.24 ± 0.13, 52	−0.10 ± 0.13, 52
age (V13)	−0.53 ± 0.10, 51	0.02 ± 0.16, 51	0.06 ± 0.14, 49	−0.49 ± 0.11, 49	−0.23 ± 0.14, 49
[Fe/H]	0.67 ± 0.08, 56	−0.08 ± 0.15, 56	−0.08 ± 0.15, 54	0.45 ± 0.13, 53	0.47 ± 0.12, 53
M_V	−0.43 ± 0.12, 56	−0.63 ± 0.09, 56	0.72 ± 0.07, 54	−0.38 ± 0.13, 53	−0.59 ± 0.10, 53
$\log\mathcal{M}/\mathcal{M}_\odot$	0.58 ± 0.14, 43	0.64 ± 0.09, 43	−0.81 ± 0.05, 43	0.41 ± 0.13, 42	0.72 ± 0.09, 42
f_{bin}^{C}	0.17 ± 0.17, 34	−0.36 ± 0.14, 34	0.50 ± 0.17, 33	−0.02 ± 0.20, 33	−0.08 ± 0.19, 33
f_{bin}^{C-HM}	−0.11 ± 0.16, 46	−0.43 ± 0.10, 46	0.58 ± 0.11, 45	−0.08 ± 0.17, 45	−0.32 ± 0.15, 45
f_{bin}^{oHM}	−0.19 ± 0.16, 41	−0.30 ± 0.14, 41	0.65 ± 0.12, 40	0.27 ± 0.16, 39	−0.32 ± 0.15, 39
$S_{RRLyrae}$	−0.25 ± 0.13, 56	−0.15 ± 0.14, 56	−0.08 ± 0.14, 54	0.17 ± 0.14, 55	−0.13 ± 0.13, 53
$E(B-V)$	0.37 ± 0.13, 56	0.19 ± 0.16, 55	0.11 ± 0.14, 54	0.07 ± 0.15, 53	0.29 ± 0.29, 53
N_1/N_{TOT}	−0.36 ± 0.13, 53	−0.49 ± 0.11, 52	1.00, 54	−0.25 ± 0.14, 53	−0.59 ± 0.10, 53

6.1 RGB width and global cluster parameters

Table 3 lists the Spearman's rank correlation coefficients of the $W_{C\,F275W,\,F336W,\,F438W}$ RGB width with all the GC global parameters just listed above. The table also provides the number of clusters used for each determination of r, given in each column after the error on r. There is no significant correlation between the intrinsic RGB width and most of the global parameters, but a strong correlation ($r = 0.79 \pm 0.05$) exists between $W_{C\,F275W,\,F336W,\,F438W}$ and metallicity, as shown in the left-hand panel of Fig. 20. This is hardly surprising, as at low metallicity the RGB colours become almost insensitive to metal abundances while the RGB-colour sensitivity to composition increases with increasing metallicity.

There is only a mild correlation between the RGB width and the cluster absolute luminosity ($r = -0.38 \pm 0.12$), when using the entire sample of GCs, as shown in the right-hand panel of Fig. 20. However, we note that GCs with almost the same [Fe/H] exhibit quite different $W_{C\,F275W,\,F336W,\,F438W}$ values, thus suggesting that at least one more parameter is controlling the RGB width. Indeed, in the left-hand panel of Fig. 20 we have marked with red dots GCs

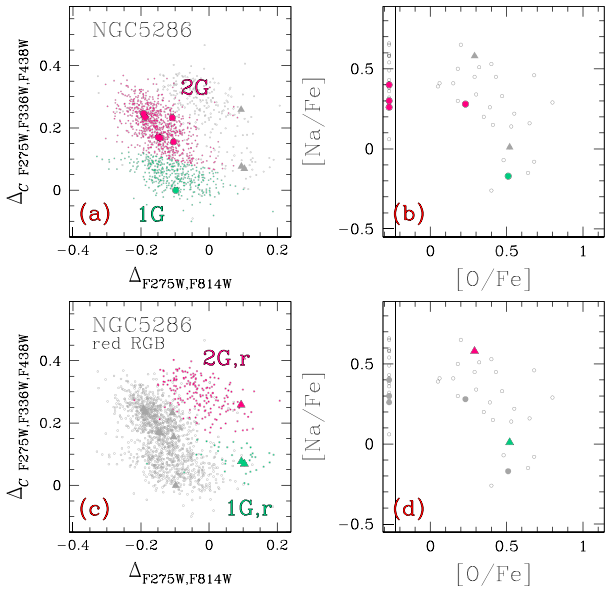

Figure 19. In the chromosome map of NGC 5286, shown in panel (a) only stars from the blue-RGB are used, i.e. those coloured black in Fig. 12. Aqua and magenta colours highlight 1G and 2G stars, respectively, with stars also studied spectroscopically are represented by large filled symbols and whose [Na/Fe] versus [O/Fe] plot from Marino et al. (2015) is shown in panel (b). Finally, in panel (c) the red-RGB stars are coloured either aqua or red for being considered the first or the second generation (1G,r and 2G,r) of the iron-rich population, while panel (d) shows the corresponding [Na/Fe] versus [O/Fe] from Marino et al. (2015).

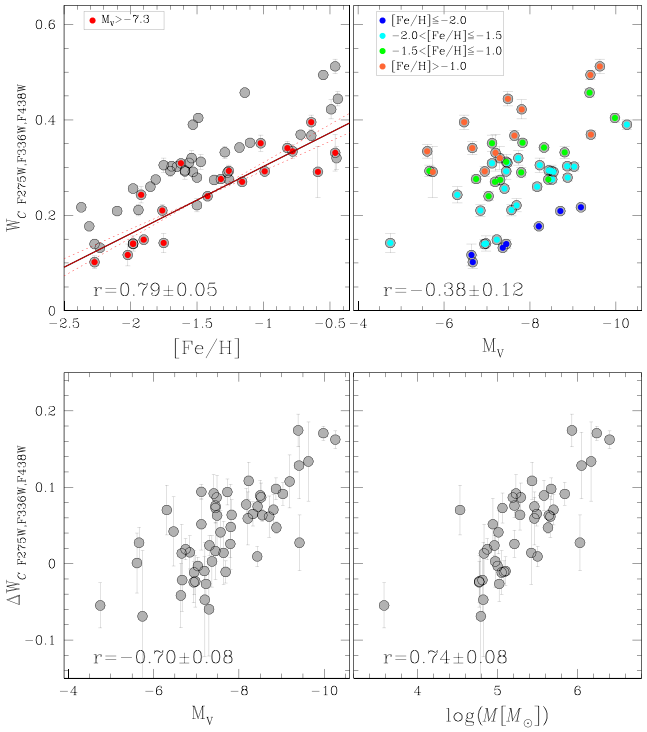

Figure 20. Upper-left panel: the intrinsic RGB width, $W_{C\,F275W,\,F336W,\,F438W}$, as a function of the iron abundance of the host GCs. The red line is the least-squares best-fitting for the faint, less massive clusters with absolute magnitude $M_V > -7.3$, that are marked with red dots. Upper-right panel: the $W_{C\,F275W,\,F336W,\,F438W}$ RGB width versus the absolute visual magnitude M_V of the host clusters. Clusters are colour-coded depending on their metallicity [Fe/H] as indicated in the insert. Lower panels: the residuals of the RGB width, $\Delta W_{C\,F275W,\,F336W,\,F438W}$, against the absolute magnitude (left) and the mass (right) of the host clusters. The Spearman's rank correlation coefficient (r) and the corresponding uncertainty are reported in each panel.

fainter than $M_V > -7.3$. Clearly the RGB width also depends on the cluster luminosity (or mass).

Low-mass clusters clearly exhibit, on average, smaller $W_{C\,F275W,\,F336W,\,F438W}$ values than more luminous, more massive GCs and define a tighter $W_{C\,F275W,\,F336W,\,F438W}$ versus [Fe/H] correlation ($r = 0.85 \pm 0.07$). The significance of the correlation between RGB width and M_V becomes evident when distinguishing different metallicity ranges, as done in the right-hand panel of Fig. 20. We found $r = 0.76 \pm 0.13$ and $r = 0.82 \pm 0.11$ for the selected groups of metal-rich and metal-poor GCs, respectively, and $r = 0.73 \pm 0.10$ for GCs with $-2.0 <$ [Fe/H] ≤ -1.5. The correlation coefficient has lower values for metal-intermediate GCs with $-1.5 <$ [Fe/H] ≤ -1.0 and corresponds to $r = 0.45 \pm 0.22$.

To further investigate the correlation between the width $W_{C\,F275W,\,F336W,\,F438W}$ and global cluster parameters, we need to remove the dependence on metallicity. Thus, we have least-squares fitted the $W_{C\,F275W,\,F336W,\,F438W}$ versus [Fe/H] relation for GCs with $M_V > -7.3$ with a straight line, as shown in the left-hand panel of Fig. 20, where the best-fitting line is given by $W_{C\,F275W,\,F336W,\,F438W} = 0.14 \pm 0.02$ [Fe/H]$+0.44 \pm 0.03$. We have then calculated the residuals $\Delta W_{C\,F275W,\,F336W,\,F438W}$ with respect to this line. The values of the resulting Spearman's rank correlation coefficient are listed in Table 3 for each relation involving $\Delta W_{C\,F275W,\,F336W,\,F438W}$. As expected, $\Delta W_{C\,F275W,\,F336W,\,F438W}$ strongly correlates with the absolute luminosity and with the cluster mass (lower panels of Fig. 20 ($r > 0.7$).

The $W_{F275W,\,F814W}$ RGB width has then been analysed in close analogy with what done for $W_{C\,F275W,\,F336W,\,F438W}$. As reported in Table 3, there is a positive correlation between $W_{C\,F275W,\,F814W}$ and the cluster metallicity ($r = 0.65 \pm 0.08$), see also the left-hand panel of Fig. 21, where the less massive clusters with $M_V > -7.3$ are marked with red dots. The least-squares best-fitting straight line for the group of GCs with $M_V > -7.3$ is plotted in red in the left-hand panel of Fig. 21 and the residuals $\Delta W_{F275W,\,F814W}$ with respect to such line are plotted as a function of cluster luminosity and mass in the two panels on the right of the same figure. Strong correlations of such residuals with cluster luminosity and mass are quite evident. We have investigated the relation between $\Delta W_{F275W,\,F814W}$ and the other global cluster parameters, but no other significant correlation appears to exist, as reported in Table 3.

6.2 Fraction of 1G stars and global cluster parameters

In this section, we investigate univariate relations between the population ratio N_1/N_{TOT} and the global parameters of the host GCs, in analogy with what has been done for the RGB width. The results are reported in Table 3.

The most relevant result is plotted in Fig. 22, which shows significant anticorrelations between the N_1/N_{TOT} ratio and the absolute luminosity and mass of the host clusters (with $r = -0.72 \pm 0.07$ and $r = -0.81 \pm 0.05$, respectively), with more massive GCs having, on average, a smaller fraction of 1G stars. Based on a more limited data set, it had been previously claimed that there is no correlation between the population ratio and cluster mass (Bastian & Lardo 2015). On the contrary, the N_1/N_{TOT} ratio correlates or anticorrelates with several quantities that are closely related with the cluster luminosity and mass. The values of the Spearman's rank correlation

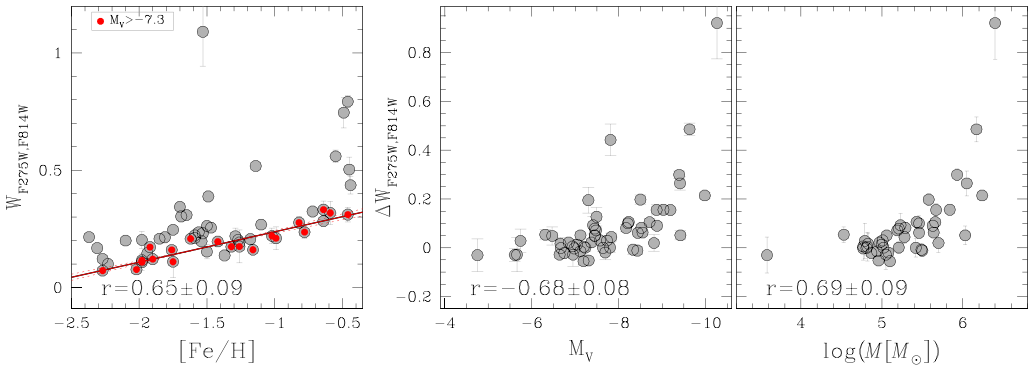

Figure 21. The left-hand panel shows the intrinsic RGB width, $W_{F275W,\,F814W}$, as a function of metallicity of the host GC. The red line is the best-fitting straight line for clusters with $M_V > -7.3$ that we have represented with red dots. The residuals of the RGB width with respect to the best-fitting line, $\Delta W_{F275W,\,F814W}$, are plotted against the absolute visual magnitude and the cluster mass in the middle and the right-hand panels, respectively. The Spearman's rank correlation coefficient and the corresponding uncertainty are reported in each panel. The outlier point refers to ω Centauri.

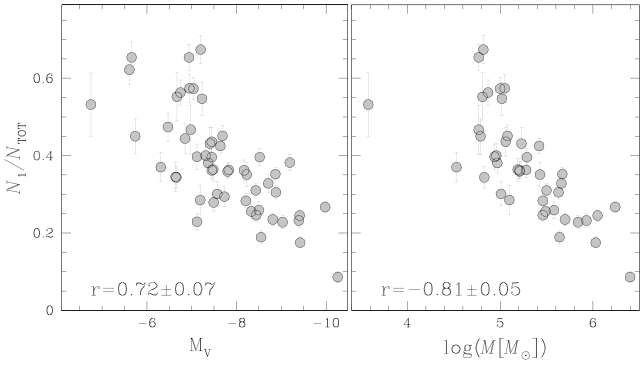

Figure 22. The fraction of 1G stars with respect of the total number of used RGB stars as a function of the cluster absolute luminosity (left), cluster mass (right).

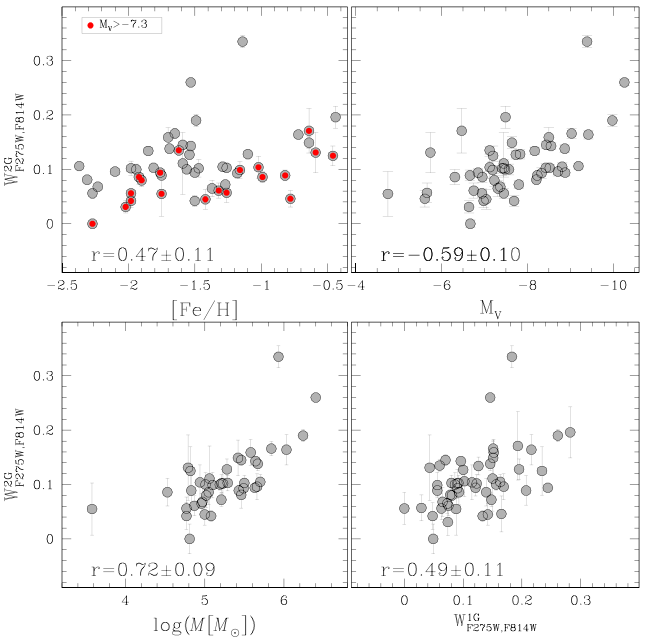

Figure 23. The intrinsic width $W^{2G}_{F275W,F814W}$ of the 2G stars as a function of cluster metallicity and absolute magnitude (upper-left and -right panels, respectively), and as a function of the cluster mass and of the intrinsic width of 1G stars (lower-left and -right panels, respectively). Symbols are like in Fig. 20. The Spearman's rank correlation coefficient and the corresponding uncertainty are indicated in each panel.

coefficient listed in Table 3 indicate a significant correlation with the central surface brightness (μ_V, in mag arcsec^{-2}, $r = 0.71 \pm 0.07$) and significant anticorrelations with the central stellar density ρ_0 ($r = -0.63 \pm 0.09$) and the central velocity dispersion σ_v ($r = -0.63 \pm 0.09$).

We find no significant correlations between the fraction of 1G stars and other global parameters, in particular between the population ratio and the distance from the Galactic centre ($r = -0.05 \pm 0.13$) or with the cluster metallicity ($r = -0.08 \pm 0.15$).

6.3 The $\Delta_{F275W,\,F814W}$ colour extension of 1G and 2G stars and global cluster parameters

We did not find any strong correlation between $W^{1G}_{F275W,F814W}$ and any of the parameters that we have investigated. There is some mild correlation ($r \sim 0.5$) with the GC metallicity, the cluster mass, and with GC ages ($r = -0.49 \pm 0.11$), but only when ages from Vandenberg et al. (2013) are used. In summary, it is still unclear what controls the $\Delta_{F275W,\,F814W}$ extension of 1G stars.

In contrast, as shown in Fig. 23, $W^{2G}_{F275W,F814W}$ correlates with cluster mass and luminosity. Moreover, there is some anticorrelation with the fraction of 1G stars ($r = 0.59 \pm 0.10$), which indicates that clusters with a predominant 2G also have wide RGB width in the $F275W-F814W$ colour. There is no strong correlation between $W^{2G}_{F275W,F814W}$ and the cluster metallicity ($r = 0.35 \pm 0.11$), although metal-rich GCs with $M_V > -7.3$ have on average larger values of $W^{2G}_{F275W,F814W}$ than metal-poor clusters within the same luminosity range. Similarly, there is only a mild correlation between the extension of the two generations, $W^{2G}_{F275W,F814W}$ and $W^{1G}_{F275W,F814W}$ ($r = 0.49 \pm 0.11$).

7 SUMMARY AND CONCLUSIONS

We have analysed high-precision multiband *HST* photometry of 57 GCs in order to identify and characterize their multiple stellar populations along the RGB. The photometry has been collected through the *F275W*, *F336W*, *F438W* filters of WFC3/UVIS and the

*F*606*W* and *F*814*W* filters of WFC/ACS mostly as part of the *HST* UV Legacy Survey of Galactic GCs (Paper I). Archive data have also been used. The main results can be summarized as follows.

(i) From the m_{F814W} versus $C_{F275W,\,F336W,\,F438W}$ pseudo-CMD and the m_{F814W} versus $m_{F275W} - m_{F814W}$ CMD of each cluster, which are both very sensitive to multiple stellar populations, we have calculated the RGB width in $C_{F275W,\,F336W,\,F438W}$ ($W_{C\,F275W,\,F336W,\,F438W}$) and in $m_{F275W} - m_{F814W}$ ($W_{F275W,\,F814W}$). In all 57 GCs, the observed RGB width is significantly wider than expected from observational errors alone. This demonstrates that none of the studied GCs is consistent with hosting a simple stellar population. Among them, ω Centauri, ($M = 10^{6.40}\,M_{\odot}$) and NGC 6535 ($M = 10^{3.58}\,M_{\odot}$) are, respectively, the most massive and the least-massive GC of the sample where multiple stellar populations have been detected to date.

(ii) For each cluster we have combined the $C_{F275W,\,F336W,\,F438W}$ pseudo-colour and of the $m_{F275W} - m_{F814W}$ colour to construct the $\Delta_{C\,F275W,\,F336W,\,F438W}$ versus $\Delta_{F275W,\,F814W}$ pseudo-two-colour diagram, or 'chromosome map', which maximizes the information on multiple stellar populations.

(iii) The chromosome maps of the majority of the GCs shows two major, well-separated groups of stars that we identify with first and second generation (1G and 2G). 1G stars are distributed around the origin of the chromosome map and span a narrow range of $\Delta_{C\,F275W,\,F336W,\,F438W}$ values. The group of 2G stars that includes the remaining RGB stars span a wide range of both $\Delta_{C\,F275W,\,F336W,\,F438W}$ and $\Delta_{F275W,\,F814W}$ values. Such a clean 1G/2G separation is not possible for a few GCs (namely, NGC 5927, NGC 6304, and NGC 6441), where the two sequences appear to be inextricably merged into a single sequence. Collectively, these clusters (with or without a clear 1G/2G separation) are called type-I clusters.

(iv) The chromosome maps of a second group of clusters, called type-II clusters, show a more complex pattern, with an apparent split of both 1G and 2G sequences. A careful examination of multiband CMDs of all these clusters reveals that their SGBs are split also in purely optical CMDs, while the SGB of type-I GCs splits only in CMDs based on ultraviolet filters. By using spectroscopic data from the literature, we showed that type-II clusters host populations that are also enriched in overall CNO abundance (C+N+O) and heavy elements, such as iron and s-process elements. In particular, it is shown that the faint SGB corresponds to the stellar population enhanced in heavy elements (e.g. Marino et al. 2011). We argue that (1) split 1G and 2G sequences in the chromosome maps, (2) split SGBs, and (3) non-uniformity of the iron and s-elements abundances must be physically connected to each other. This evidence indicates that chromosome maps are an efficient tool to identify GCs with internal variations of heavy elements. In this way, we have identified two new type-II GCs, namely NGC 1261 and NGC 6934.

(v) We use spectroscopic evidence from the literature to show that the photometrically selected 1G and 2G stars are oxygen-rich and sodium-poor and oxygen-poor and sodium-rich, respectively, supporting our identification of 1G and 2G stars with the first and second stellar generation, respectively. However, the number of stars with both accurate *HST* multiband photometry and spectroscopic chemical analysis is still quite scanty. An extensive chemical tagging of multiple populations identified on the chromosome maps is now becoming a major requirement to further progress in the field of stellar populations in GCs.

(vi) Noticeably, the colour width of both 1G and 2G stars in most GCs is significantly wider than what observational errors would suggest. Such evidence demonstrates that in most GCs even the first (1G) stellar generation is not consistent with a simple, chemically homogeneous stellar population. Again, spectroscopic chemical tagging of 1G stars is needed to identify the origin of their wide range of $\Delta_{F275W,\,F814W}$ values.

(vii) We have investigated univariate relations between the RGB width in the $W_{F275W,\,F814W}$ colour and in the $W_{C\,F275W,\,F336W,\,F438W}$ pseudo-colour and the main global parameters of the host GCs. The RGB width mostly correlates with cluster metallicity. After removing the dependence on metallicity, significant correlations emerge between the RGB width and cluster mass and luminosity. These results indicate that massive GCs exhibit more pronounced internal variations of helium and light elements compared with low-mass GCs.

(viii) For each cluster the *F*275*W*−*F*814*W* colour width of 1G and 2G stars ($W^{1G(2G)}_{F275W,\,F814W}$) have been measured. No significant correlation has been recovered between $W^{1G}_{F275W,\,F814W}$ and any of the global cluster parameters. In contrast $W^{2G}_{F275W,\,F814W}$ correlates with the cluster mass.

(ix) We have measured the fraction of 1G RGB stars with respect to the total number of RGB stars. The N_{1G}/N_{TOT} ratio ranges from ∼0.08 in the case of ω Centauri to ∼0.67. There is a significant anticorrelation between the fraction of 1G stars and the mass of the host cluster, with massive GCs hosting a smaller fraction of 1G stars. Hence, the multiple population phenomenon appears to systematically increase in incidence and complexity with increasing cluster mass.

(x) In some cases distinct stellar clumps are clearly present along the sequence of 1G and/or 2G stars, while in other clusters we observe a smooth distribution without evident clumps. However, a large number of stars is needed to unambiguously identify distinct subpopulations along the MSs in the chromosome maps, as done in Paper II and Paper III for NGC 7089 and NGC 2808, respectively.

ACKNOWLEDGEMENTS

Support for *Hubble Space Telescope* proposal GO-13297 was provided by NASA through grants from Space Telescope Science Institute (STScI), which is operated by Association of Universities for Research in Astronomy (AURA), Inc., under National Aeronautics and Space Administration (NASA) contract NAS 5-26555. We thank the anonymous referee for her/his suggestions that have improved the quality of the paper. APM and AFM acknowledge support by the Australian Research Council through Discovery Early Career Researcher Awards DE150101816 and DE160100851. GP, AR, FD, and SC acknowledge financial support by PRIN-INAF2014 (PI: Cassisi).

REFERENCES

Anderson J., Bedin L. R., 2010, PASP, 122, 1035
Anderson J., King I. R., 2003, AJ, 126, 772
Anderson J., King I. R., 2006, Instrument Science Report ACS 2006-01, 1
Anderson J. et al., 2008, AJ, 135, 2055
Bastian N., Lardo C., 2015, MNRAS, 453, 357
Bedin L. R., Piotto G., Anderson J., Cassisi S., King I. R., Momany Y., Carraro G., 2004, ApJ, 605, L125
Bedin L. R., Cassisi S., Castelli F., Piotto G., Anderson J., Salaris M., Momany Y., Pietrinferni A., 2005, MNRAS, 357, 1038
Bellini A., Piotto G., Bedin L. R., King I. R., Anderson J., Milone A. P., Momany Y., 2009, A&A, 507, 1393

Bellini A., Anderson J., Bedin L. R., 2011, PASP, 123, 622
Bellini A. et al., 2013, ApJ, 765, 32
Bellini A. et al., 2015, ApJ, 810, L13
Brown T. M. et al., 2016, ApJ, 822, 44
Carretta E., Bragaglia A., Gratton R. G., Leone F., Recio-Blanco A., Lucatello S., 2006, A&A, 450, 523
Carretta E. et al., 2009, A&A, 505, 117
Carretta E., Gratton R. G., Bragaglia A., D'Orazi V., Lucatello S., 2013, A&A, 550, A34
Cassisi S., Salaris M., Pietrinferni A., Piotto G., Milone A. P., Bedin L. R., Anderson J., 2008, ApJ, 672, L115
Cordero M. J., Pilachowski C. A., Johnson C. I., McDonald I., Zijlstra A. A., Simmerer J., 2014, ApJ, 780, 94
D'Antona F., Vesperini E., D'Ercole A., Ventura P., Milone A. P., Marino A. F., Tailo M., 2016, MNRAS, 458, 2122
Decressin T., Meynet G., Charbonnel C., Prantzos N., Ekström S., 2007, A&A, 464, 1029
Dotter A. et al., 2010, ApJ, 708, 698 (D10)
Gilliland R. L., 2004, Instrument Science Report ACS 2004-01, 17
Han S.-I., Lee Y.-W., Joo S.-J., Sohn S. T., Yoon S.-J., Kim H.-S., Lee J.-W., 2009, ApJ, 707, L190
Harris W. E., 1996, AJ, 112, 1487
Ivans I. I., Sneden C., Kraft R. P., Suntzeff N. B., Smith V. V., Langer G. E., Fulbright J. P., 1999, AJ, 118, 1273
Johnson C. I., Pilachowski C. A., 2010, ApJ, 722, 1373
Johnson C. I., Rich R. M., Pilachowski C. A., Caldwell N., Mateo M., Bailey J. I., III, Crane J. D., 2015, AJ, 150, 63
McLachlan G., Peel D., 2000, Finite Mixture Models, Wiley, New York
McLaughlin D. E., van der Marel R. P., 2005, ApJS, 161, 304
Marín Franch A. et al., 2009, ApJ, 694, 1498 (MF09)
Marino A. F., Villanova S., Piotto G., Milone A. P., Momany Y., Bedin L. R., Medling A. M., 2008, A&A, 490, 625
Marino A. F., Milone A. P., Piotto G., Villanova S., Bedin L. R., Bellini A., Renzini A., 2009, A&A, 505, 1099
Marino A. F. et al., 2011, A&A, 532, A8
Marino A. F. et al., 2012, ApJ, 746, 14
Marino A. F. et al., 2015, MNRAS, 450, 815
Milone A. P., 2015, MNRAS, 446, 1672
Milone A. P. et al., 2008, ApJ, 673, 241
Milone A. P., Piotto G., Bedin L. R., Cassisi S., Anderson J., Marino A. F., Pietrinferni A., Aparicio A., 2012a, A&A, 537, A77
Milone A. P. et al., 2012b, ApJ, 744, 58
Milone A. P. et al., 2013, ApJ, 767, 120
Milone A. P. et al., 2014, ApJ, 785, 21
Milone A. P. et al., 2015a, MNRAS, 447, 927 (Paper II)
Milone A. P. et al., 2015b, ApJ, 808, 51 (Paper III)
Nardiello D. et al., 2015, MNRAS, 451, 312
Piotto G. et al., 2012, ApJ, 760, 39
Piotto G., Milone A. P., Marino A. F., Bedin L. R., Anderson J., Jerjen H., Bellini A., Cassisi S., 2013, ApJ, 775, 15
Piotto G. et al., 2015, AJ, 149, 91 (Paper I)
Renzini A. et al., 2015, MNRAS, 454, 4197
Rich R. M. et al., 1997, ApJ, 484, L25
Sarajedini A. et al., 2007, AJ, 133, 1658
Silverman B. W., 1986, Monographs on Statistics and Applied Probability. Chapman and Hall, London
Sollima A., Ferraro F. R., Bellazzini M., Origlia L., Straniero O., Pancino E., 2007, ApJ, 654, 915
Trager S. C., King I. R., Djorgovski S., 1995, AJ, 109, 218
VandenBerg D. A., Brogaard K., Leaman R., Casagrande L., 2013, ApJ, 775, 134 (V13)
Ventura P., Caloi V., D'Antona F., Ferguson J., Milone A., Piotto G. P., 2009, MNRAS, 399, 934
Villanova S., Geisler D., Gratton R. G., Cassisi S., 2014, ApJ, 791, 107
Wilson C. P., 1975, AJ, 80, 175
Yong D., Grundahl F., D'Antona F., Karakas A. I., Lattanzio J. C., Norris J. E., 2009, ApJ, 695, L62
Yong D. et al., 2014, MNRAS, 441, 3396
Yong D., Da Costa G. S., Norris J. E., 2016, MNRAS, 460, 1846

APPENDIX A: THE CONSTRUCTION OF THE CHROMOSOME MAP OF ω CENTAURI

ω Centauri shows the most complex chromosome map. The distribution of the stars that we have coloured black in Fig. 6 resembles that of some GCs with single SGB like NGC 6723 or NGC 2808. In contrast, red-RGB stars exhibit an unique pattern, with three main streams of red-RGB stars. The most populous RGB starts from ($\Delta_{F275W,\,F814W}$; $\Delta_{F275W,\,F336W,\,F438W}$) $\sim$ (−0.2; 0.35) and extends towards extreme values of $\Delta_{F275W,\,F814W} \sim 1.5$. A second stream ranges from ($\Delta_{F275W,\,F814W}$; $\Delta_{F275W,\,F336W,\,F438W}$) $\sim$ (0.0; 0.1) to (1.5; −0.4) and possibly includes a few stars with even larger $\Delta_{F275W,\,F814W}$. A third stream has intermediate $\Delta_{F275W,\,F814W}$ and $\Delta_{F275W,\,F336W,\,F438W}$ values with respect to the previous two.

Each stream includes substellar populations. In an attempt to estimate how many groups of stars are statistically significant in ω Centauri, we used the MCLUSTER CRAN package in the public domain R statistical software system. This package performs a maximum likelihood fits to different number of stellar groups by using several different assumptions about shape and size of the different populations in the chromosome map, and evaluate the number of groups by the Bayesian Information Criterion (BIC) penalized likelihood measure for model complexity (see McLachlan & Peel 2000, for details). For each shape and size that we adopted for the populations, we assumed a number, N, of stellar populations from 1 to 20 and estimated a BIC for each combination. The best BIC value corresponds to $N = 16$.

When compared with the other GCs investigated in this paper, ω Centauri exhibits by far the most complex CMD and its RGB spans a very wide range of $m_{F275W} - m_{F814W}$ colour as shown in panel (a1) of Fig. A1. Due to the complex structure of its RGB, in order to derive the chromosome map of ω Centauri, we have adopted an iterative procedure that is based on the method of Section 3.2, and which is illustrated in Fig. A1.

As a first step, we have derived a raw chromosome map by using the same procedure described in Section 3.2. Then, we have identified three groups of stars that have been used to derive the fiducial lines shown in m_{F814W} versus $m_{F275W} - m_{F814W}$ CMD and the m_{F814W} versus $C_{F275W,\,F336W,\,F438W}$ pseudo-CMD plotted in panels (a1) and (b1) of Fig. A1. The selected groups of stars are shown in panels (c) and (d) of Fig. A1 where black and orange dots and aqua-starred symbols overimposed on the final chromosome map of ω Centauri represent stars of the samples 1, 2, and 3, respectively.

These three groups of stars have been determined iteratively by using the following criteria. The chromosome map of stars in sample 1 resembles those observed in several GCs in which the stars are distributed along a single sequence and define distinct bumps. Sample 2 includes the bump of stars around ($\Delta_{F275W,\,F814W}$;$\Delta_{F275W,\,F336W,\,F438W}$) $\sim$ (−1.10; 0.35), while sample 3 includes most of the stars of the reddest and the most metal-rich RGB of ω Centauri that has been often indicated as population a (e.g. Bedin et al. 2004). Noticeably, we have excluded from sample 3 the stars in the poorly populated bump with ($\Delta_{F275W,\,F814W}$; $\Delta_{F275W,\,F336W,\,F438W}$) $\sim$ (0.3; 0.0).

In order to derive $\Delta_{F275W,\,F814W}$ for RGB stars in ω Centauri, we have used the following procedure that is illustrated in panels (a1) and (a2) of Fig. A1. We have first divided the RGB stars in three groups. Group I includes all the RGB stars with bluer $m_{F275W} - m_{F814W}$ colours than the red fiducial line at the corresponding

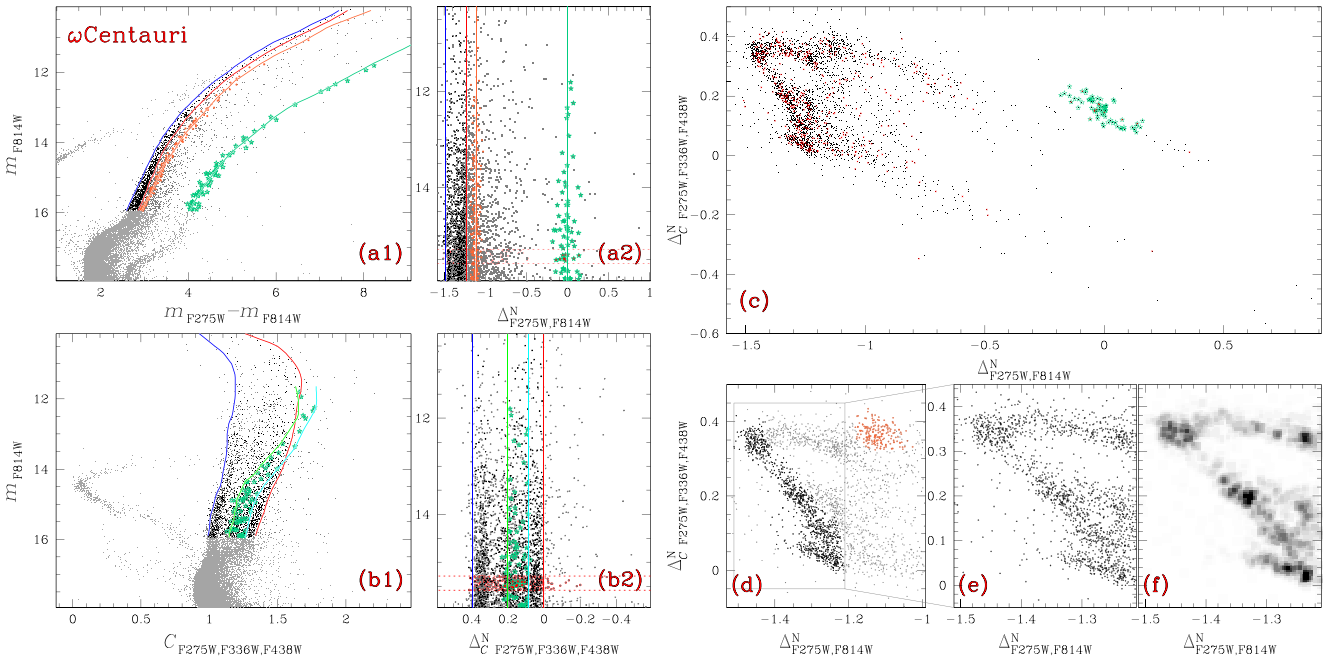

Figure A1. This figure illustrates the procedure used to derive the chromosome map of NGC 5139 (ω Centauri). The m_{F814W} versus $m_{F275W} - m_{F814W}$ CMD and the m_{F814W} versus $C_{F275W,\,F336W,\,F438W}$ pseudo-CMD are plotted in panels (a1) and (b1), respectively. Dark-grey and coloured points to mark the sample of analysed RGB stars. The red and the blue lines overimposed on the diagrams of both panels (a1) and (d1) correspond to the red and the blue envelopes of RGB of stars in the sample 1. The orange and the green lines shown in the panel (a1) are the fiducial lines of the samples 2 and 3 of stars. In the panel (b1), we have used green and cyan colours to mark the red and blue edges of the envelope of RGB of sample-3 stars. Panels (a2) and (b2) show the verticalized m_{F814W} versus $\Delta_{F275W,\,F814W}$ and m_{F814W} versus $\Delta_{C\,F275W,\,F336W,\,F438W}$ diagrams for RGB stars. The $\Delta_{C\,F275W,\,F336W,\,F438W}$ versus $\Delta_{F275W,\,F814W}$ chromosome map of RGB stars in ω Centauri is shown in panel (c), where red dots represent RGB stars with $15.28 < m_{F814W} < 15.58$ between the two horizontal dotted lines of panels (a2) and (b2). Panels (d) and (e) are zoomed-in view of the chromosome map shown in panel (c), while panel (f) shows the $\Delta_{F275W,\,F336W,\,F438W}$ versus $\Delta_{F275W,\,F814W}$ Hess diagram of the stars plotted in panel (e). The aqua-starred symbols plotted in panels (a1), (a2), (b1), (b2), and (c) mark the sample-3 stars, while sample-1 stars are represented with black dots in panels (a1), (a2), (b1), (b2), and (d). The orange dots shown in panels (a1), (a2), and (d) indicate sample-2 stars.

$F814W$ magnitude. Group II includes the RGB stars between the red and the orange line, while the remaining RGB stars belong to group III. The red and the blue fiducial lines shown in panel (a1) are the redder and the bluer envelopes of the RGB formed by sample-1 stars and have been derived as in Section 3.1 by using sample-1 stars only. The orange and the aqua lines shown in panel (a1) are fiducial lines of the RGB made by sample-2 and sample-3 stars. We have derived the quantities $\Delta^{\rm N\,I}_{F275W,F814W}$, $\Delta^{\rm N\,II}_{F275W,F814W}$, and $\Delta^{\rm N\,III}_{F275W,F814W}$ for stars in the three groups, by using the following equations that are similar to equation (1):

$$\Delta^{\rm N\,I(II,III)}_{F275W,F814W} = W^{\rm I,(II,III)}_{F275W,F814W} \times[(X - X_{\rm fiducialA})/(X_{\rm fiducialB} - X_{\rm fiducialA})]. \quad \text{(A1)}$$

For group-I stars, we have assumed the blue and the red fiducial shown in panel (a1) of Fig. A1 as the fiducial A and fiducial B, respectively. For group-II stars, the red fiducial corresponds to fiducial A and the orange fiducial corresponds to fiducial B, while for group-III stars we used the orange and the green fiducials as fiducial A and B, respectively. The constant $W^{\rm I}_{F275W,F814W}$ has been derived for group-I stars as in Section 3.1, while $W^{\rm II}_{F275W,F814W}$ has been derived as the $m_{F275W} - m_{F814W}$ colour difference between the orange and the red fiducial line shown in panel (a1) of Fig. A1 calculated 2.0 $F814W$ mag above the MS turnoff. The constant $W^{\rm III}_{F275W,F814W}$ has been derived similarly for group-III star, but by using green and orange fiducials.

We assumed:
$\Delta_{F275W,F814W} = \Delta^{\rm N\,I}_{F275W,F814W}$ for group-I stars;
$\Delta_{F275W,F814W} = W^{\rm I}_{F275W,F814W} + \Delta^{\rm N\,II}_{F275W,F814W}$ for group-II stars; and
$\Delta_{F275W,F814W} = W^{\rm I}_{F275W,F814W} + W^{\rm II}_{F275W,F814W} + \Delta^{\rm N\,III}_{F275W,F814W}$ for group-III stars. The verticalized m_{F814W} versus $\Delta_{F275W,\,F814W}$ diagram of the analysed RGB stars in ω Centauri is plotted in the panel (a2) of Fig. A1 where the vertical coloured lines corresponds to the fiducial lines shown in panel (a1).

In order to derive $\Delta_{C\,F275W,\,F336W,\,F438W}$ for RGB stars of ω Centauri we adopted the method illustrated in panels (b1) and (b2) of Fig. A1, where the red and blue lines are the boundaries of the RGB for stars in sample 1, while the green and the cyan lines are the boundaries for stars in the sample 3. These lines have been derived as described in Section 3.1.

We proceeded by defining two additional groups of stars. Group IV includes all the RGB stars that are associated with the most metal-rich population of ω Centauri and that have $\Delta_{F275W,\,F814W} > -0.2$ and $\Delta_{C\,F275W,\,F336W,\,F438W} > -0.1$ in panel (c) of Fig. A1. Group V includes all the remaining RGB stars.

We derived $\Delta^{\rm N,IV}_{C\;F275W,F336W,F438W}$ for group-IV stars by means of equation (2) and by assuming the green and cyan lines plotted in panel (b1) of Fig. A1 as fiducials A and B, respectively. Similarly, we have calculated $\Delta^{\rm N,V}_{C\;F275W,F336W,F438W}$ by using equation (2) and assuming that the blue and red lines in the panel (b1) of Fig. A1 correspond to the fiducials A and B, respectively.

We assumed:
$\Delta_{C\ F275W,F336W,F438W} = \Delta^{\rm N,IV}_{C\ F275W,F336W,F438W}$ for group-IV stars and;
$\Delta_{C\ F275W,F336W,F438W} = W^{\rm IV-V}_{C\ F275W,F336W,F438W} + \Delta^{\rm N,V}_{C\ F275W,F336W,F438W}$ for group-V stars, where $W^{\rm IV-V}_{C\ F275W,F336W,F438W}$ is the $C_{F275W,F336W,F438W}$ pseudo-colour difference between the blue and the cyan fiducial line calculated 2.0 $F814W$ magnitudes above the MS turnoff.

The chromosome map has been derived iteratively and four iterations were required to reach convergence. After each iteration, we improved the selection of stars in the samples 1, 2, and 3, derived improved fiducial lines and better estimates of $\Delta_{F275W,F814W}$ and $\Delta_{C\,F275W,F336W,F438W}$.

The chromosome map of ω Centauri is plotted in the panel (c) of Fig. A1 and it reveals a very complex stellar distribution, with the presence of distinct bumps of stars and stellar streams. To verify that the observed structure does not include artefacts introduced by the adopted fiducial lines, we marked in red in panel (c) all the stars in a small magnitude interval with $15.38 < m_{F814W} < 15.58$ that are placed between the horizontal dotted lines of panels (a2) and (b2). The fact that the selected stars distribute along the entire map demonstrates that the observed stellar bumps and tails are real. Panels (d) and (e) of Fig. A1 are a zoomed-in view of the chromosome map around the region with low values of $\Delta_{F275W,F814W}$, while panel (f) shows the Hess diagram of the same stars plotted in panel (e). These figures reveal that the sample 1 of stars in ω Centauri define a continuous sequence characterized by the presence of distinct stellar bumps, in close analogy with what we observe in NGC 6723. In addition, ω Centauri hosts stellar populations, including bumps and streams, with values of $\Delta_{F275W,F814W}$ larger than those of sample-1 stars with the same $\Delta_{F275W,F336W,F438W}$.

This paper has been typeset from a TEX/LATEX file prepared by the author.